POLITECNICO DI TORINO
Repository ISTITUZIONALE

A comparative analysis of GIS-based tools for accurate photovoltaic potential prediction at urban scale

Original
A comparative analysis of GIS-based tools for accurate photovoltaic potential prediction at urban scale / Anselmo, S., Martinez, A.M., Boccardo, P., Ferrara, M.. - In: SOLAR ENERGY. - ISSN 0038-092X. - ELETTRONICO. - 318:(2026). [10.1016/j.solener.2026.115038]

Availability:
This version is available at: 11583/3017235 since: 2026-10-30T15:41:54Z

Publisher:
Elsevier Ltd

Published
DOI:10.1016/j.solener.2026.115038

Terms of use:

This article is made available under terms and conditions as specified in the corresponding bibliographic description in the repository

Publisher copyright

(Article begins on next page)

19 November 2026

Solar Energy 318 (2026) 115038

Contents lists available at ScienceDirect

Solar Energy

journal homepage: www.elsevier.com/locate/solener

A comparative analysis of GIS-based tools for accurate photovoltaic potential prediction at urban scale

Sebastiano Anselmo [a,*], Ana M. Martínez [b], Piero Boccardo [a], Maria Ferrara [c]

[a] Interuniversity Department of Regional and Urban Studies and Planning, Politecnico di Torino, Italy
[b] Joint Research Centre (JRC), European Commission, Italy
[c] Department of Energy, Politecnico di Torino, Italy

ARTICLE INFO

Keywords:
Photovoltaic potential
Solar radiation
Urban energy planning
Renewable energy sources
Energy simulation
Geographic information systems

ABSTRACT

In the current context of energy transition, there is a heightened focus on renewable energy sources. In urban environments, specific interest has been generated by photovoltaic technologies due to their ability to be integrated into roofs without requiring additional lands space. Geographic Information Systems are capable of identifying the most productive pitches and rationalising the panel installation process by estimating solar radiation accurately. Existing literature proposes studies based on different methodologies and tools, often relying on default values and simplifications. This paper aims to define a set of common and reliable input parameters, thus making it possible to compute the photovoltaic potential based on alternative open and commercial tools – embedded in QGIS and ArcGIS Pro respectively. The evaluation has been conducted on multiple temporal scales, focusing on three Areas of Interest with different characteristics. Different trends emerged, with QGIS results being correlated to the Linke turbidity factor and ArcGIS ones to the Diffuse-to-Global radiation ratio. Results are validated against PVGIS, showing a higher correlation with the QGIS tool.

1. Introduction

The context of sustainable development – originally drafted at the international level by the Brundtland report [1] – has been fostered by the Agenda 2030 [2], which introduced the Sustainable Development Goals (SDGs). SDG7 aims to "Ensure access to affordable, reliable, sustainable and modern energy for all", thus highlighting the energy transition as a key dimension of sustainability. In particular, target 7.2 points to an increase in the share of Renewable Energy Sources (RESs). The same objective appears in the European legislation, with the concepts of Renewable Energy Community and Zero Emission Building being pivoted around the use of clean energy to meet – as much as possible – the energy demand. Recent geopolitical conflicts and challenges posed by the COVID-19 pandemic have led the European Commission to implement the REPowerEU Plan [3], which targets a rethinking of the energy mix to free Europe from depending on foreign fossil fuel suppliers. A part of this plan includes the solar energy strategy [4], planning the installation of 600 GW of photovoltaic production by 2030. This strategy is divided into three main initiatives: the European Solar Rooftops Initiative – promoting the panel installation –, large-scale skills partnerships, and an industry alliance.

While the current situation has increased the urgency of the energy transition, the European Union introduced this concept in its normative body more than twenty years ago. Indeed, the first directive on the promotion of the use of energy from renewable sources [5] dates back to 2009, two years after the formal commitment by the European Council to reach a 20 % share of RES in overall EU energy consumption by 2020 [6]. One of the most relevant pushes to increase the relevance of RESs in the energy mix derives from the Fit for 55 package [7], part of the European Green Deal [8] for climate neutrality. In order to make European legislation compliant with the 2050 decarbonisation targets, it proposes the revision of several directives, among which the Renewable Energy Directive (RED) and the Energy Performance of Buildings Directive (EPBD) are the most relevant. The former [9] promotes the realisation of supporting frameworks at local and national levels, the latter [10] requires the inclusion of renewable energy in the building energy mix to reduce the non-renewable energy performance – and subsequently the CO_2 emissions. Among the RESs, photovoltaic (PV) technology obtained a special interest in the urban environments because of the possibility to integrate PV panels within roofs, resulting in lower impacts – in terms of land take and environmental costs of the installation – compared to solar farms. Based on the proximity to the consumers and the scarce space availability in urban areas, PV technology has a key role in the transition

* Corresponding author.
E-mail address: sebastiano.anselmo@polito.it (S. Anselmo).

https://doi.org/10.1016/j.solener.2026.115038
Received 29 June 2026; Received in revised form 7 August 2026; Accepted 18 August 2026
Available online 24 August 2026
0038-092X/© 2026 The Authors. Published by Elsevier Ltd on behalf of International Solar Energy Society. This is an open access article under the CC BY-NC-ND license (http://creativecommons.org/licenses/by-nc-nd/4.0/).

Nomenclature

AoI	Area of Interest
ASR	Area Solar Radiation tool
DEM	Digital Elevation Model
DG	Diffuse-to-Global radiation ratio
DSM	Digital Surface Model
DTM	Digital Terrain Model
GIS	Geographic Information System
LiDAR	Light Detection And Ranging
MAE	Mean Absolute Error
PV	Photovoltaic
PVGIS	Photovoltaic Geographical Information System
r.sun	r.sun.insoltime tool
RMSE	Root Mean Square Error
SDG	Sustainable Development Goal
SoDA	Solar radiation Database
RES	Renewable Energy Source
RSR	Raster Solar Radiation tool
TMY	Typical Meteorological Year

to green energy [11].

In order to ensure the full exploitation of the solar potential and accelerate European achievements toward RES, it is necessary to define supporting tools for planning effective PV systems. Specifically, it is crucial to avoid pitches affected by shadows or characterised by unfavourable tilt and orientation in order to maximise the productivity. This is particularly relevant in the urban context, characterised by varying heights and complex geometries. With Digital Twins – for which 3D city models are produced – emerging as relevant tools for the development of the smart city concept, three-dimensional geospatial data can be effective for identifying the buildings with the highest potential for photovoltaic production. Nevertheless, 2.5D datasets –bidimensional geospatial files including the information on the vertical component – are often preferred for computational reasons [12]. Geographic Information Systems (GIS), which feed into 2.5D and 3D datasets, are powerful software for storing, visualising and processing geographic objects. The possibility to perform complex analyses by overlapping multiple spatial layers allows to model the spatial variability of the solar radiation and compute the geometric characteristics of the potential installation surfaces – such as useful area, slope and orientation.

1.1. Scope, novelty and structure of the work

Different studies validated their results against observed data [13–15] or alternative tools [16] and databases [17], or focused on the precision of a single tool for solar radiation estimations [18]. However, with all studies employing a single software and weather input configuration, no structured comparison between the output variability in the photovoltaic potential calculation between ArcGIS Raster Solar Radiation and QGIS r.sun (short for r.sun.insoltime) has been carried out.

The scope of this study, addressing the emerging gap, is to explore the influence on the output of the selection of the software and alternative weather inputs. Resource and technical potential, two of the four levels to be addressed in energy planning according to Bódis et al. [19], are tackled in this study by considering environmental parameters and technical constraints, respectively. On the other hand, economic and market potentials are not taken into account, as they are out of the scope. Moreover, the research considers an ideal yearly production at the early stage of the PV panel lifetime: targeting the observation of differences resulting from alternative simulation tools and input configurations, it is beyond the scope of the paper to observe panel degradation or the soiling impact on the panel itself, considered in [20]. The research is divided into two parts. The first compares the inputs required by the calculation tools embedded in ArcGIS and QGIS and gathers the necessary data, and the second focuses on the differences in the outcomes from the two software tools. Validation is performed against PVGIS, a tool developed by the Joint Research Centre of the European Commission for the estimation of photovoltaic potential. The proposed approach is tested in the Metropolitan City of Turin, located in Northern Italy. Three Areas of Interest, 1 km^2 wide, have been selected for their representability.

The rest of the paper is organized as follows: Section 2 presents an overview of the state of the art. Section 3 outlines the methodology used for this comparative study, paying special attention to the different workflows required by ArcGIS and QGIS. The results of the tools are explained in the forth section, while Section 5 discusses the outcomes both quantitatively and qualitatively – by assessing the main advantages and drawbacks of the two tools and validating results. Concluding remarks pave the way for future research on the topic.

2. Literature review

Existing literature reviews on the topic of GIS-based tools for calculating the photovoltaic potential, as that by Anselmo and Ferrara [12], recognised that different studies resort to different tools and levels of simplification. The cited review highlighted how most GIS-based studies used the tools embedded in the two most widely used GIS software – ArcGIS Pro (Area Solar Radiation, updated to Raster Solar Radiation in November 2023) and QGIS (r.sun.insoltime) – to compute solar radiation. A brief explanation of tools and required inputs for solar radiation estimation is presented hereinafter.

Both tools require a Digital Elevation Model for modelling the geometries, thus casting shadows and calculating slope and orientation of the different surfaces. According to Kausika et al. [21], in urban environments, the resolution should be at least 50 cm, as varying altitudes and complex morphologies strongly affect the results. Data acquired through a Light Detection and Ranging (LiDAR) sensor are widely used for obtaining such models. As an example, the studies by Suomalainen et al. [22] and by Özdemir et al. [23] modelled geometries through this technology, resulting in high-resolution Digital Surface Models (DSMs). However, high resolution results in longer processing time. For this reason, Wong et al. [13] decided to work on a down-sampled version of a 0.5 m DSM, preferring a 3 m resolution.

Apart from the geometry, weather parameters are the other principal variable in solar radiation estimation, in particular when considering clear-sky models. In order to gather them, different alternatives are possible. First, ground-based data can be directly acquired for the purpose of the study. Different sensors, acquiring parameters such as the radiation as a whole or divided into its three components – direct, diffuse and reflected –, can be used to create a weather observatory, as proposed by Wong et al. [13]. Other scholars opt for existing databases. These can be embedded in software, as Meteonorm, used by Bayod-Rújula et al. [24]. Meteonorm is a commercial tool that also gives the possibility of using TMY3 (Typical Meteorological Year 3), built from weather data from 1020 USA locations on a 20-year time series. As the data have been interpolated to be extended to the whole world, studies both in the USA [25] and in other countries, e.g., Taiwan [26], were published. The principal example of an open database made available through a web portal is PVGIS, which was used by Hofierka and Kanuk [27] and Özdemir et al. [23]. Local authorities like ARPA Piemonte also publish their data, used by Mutani et al. [28]. When data are not available or the accuracy is considered insufficient, it is also possible to resort to existing algorithms to compute the required inputs. For instance, the SOLPOS algorithm, developed by the National Renewable Energy Laboratory, was used by Helbich et al. to compute the position of the Sun [29]. Finally, when there is no need for such high accuracy, it is possible to use the default values proposed by the software. It is the case

of the research by Suomalainen et al. [22], which used ArcGIS Area Solar Radiation default values. Note that other climatic variables such as temperature or wind speed typically considered for the estimate of photovoltaic production are not taken into consideration in QGIS or ArcGIS.

Once the incoming solar radiation on the whole urban surface is computed, it is necessary to identify the useful surfaces on which to install the panels. When classified LiDAR point clouds – returning building geometries separately from neighbouring elements – are not available, computer vision can support the roof extraction. An example is provided by Khan and Arsalan [30], who applied a six-step procedure to extract the useful roof surface from satellite pictures, segmenting the RGB imagery and applying correction factors based on shading and orientation. Besides these two parameters, additional elements have to be taken into account. First, a 1 m buffer from the edges is generally excluded as installation and maintenance area [31–33]. Second, a minimum area is required. This varies according to the geographical location and the building stock characteristics, with examples from 2 m^2 [34] to 40 m^2 [35].

For the calculation of the photovoltaic potential, different elements are to be taken into account besides the incoming solar radiation and the useful area. Two recurring elements are the Performance Ratio, defined by Mahtta et al. [36] as the ratio between performance on field and in standard conditions – thus quantifying the system losses – and the conversion efficiency of the panel. The former is generally comprised in a 75–85 % range, while the latter is made available by panel producers or synthesised in technical reviews as the solar cell efficiency tables [37]. Additionally, Liu et al. [38] introduced the life cycle of the panels, with a yearly attenuation rate equal to 0.7 %.

3. Methodology

Several methodologies can be found in the literature for the calculation of the photovoltaic potential in urban areas. Differences span from the formulas to calculate the total potential or the parameters adopted, to the tools used to compute solar radiation. The assessment of the PV potential entails the utilisation of different models – especially for the solar radiation estimation –which can be used to define the input parameters, potentially resulting in a range of alternative values to be assigned to a single parameter. This variability could have significant impacts on the ultimate outcomes of the PV potential assessment, thus requiring validation [21]. The methodology used for this research aims to compare the results obtained from the tools embedded in QGIS – r.sun.insoltime in QGIS v.3.34.11 – and ArcGIS Pro – Raster Solar Radiation in ArcGIS Pro v3.6.0, both employing clear-sky solar radiation models. To do so, the first phase consists of the creation of a dataset with monthly values from validated open-access sources. Then, several different combinations of parameters are used in both ArcGIS Pro and QGIS, to compare the variability between the outcomes of both configurations in the same software with different inputs and in different software with the same inputs.

3.1. Study areas

Three 1 km^2 Areas of Interest (AoIs) located in the Metropolitan City of Turin (Italy) were identified for the application of the methodology. The first two are located in the Municipality of Turin, while the third is located in the city of Ivrea, 45 km North-East of Turin. The localisation of the three AoIs is shown in Fig. 1.

The three AoIs – shown in Fig. 2 – are selected as reference for three alternative conditions: a strictly urban area (located in the *Barriera di Milano* neighbourhood), a sparse settlement (on the hill of Turin) and a *peri*-urban area (in Ivrea).

Turin is a medium-sized city in North-West Italy, which faced a consistent industrial boom after World War II. The sharp increase in population which followed resulted in a twofold urban expansion. On

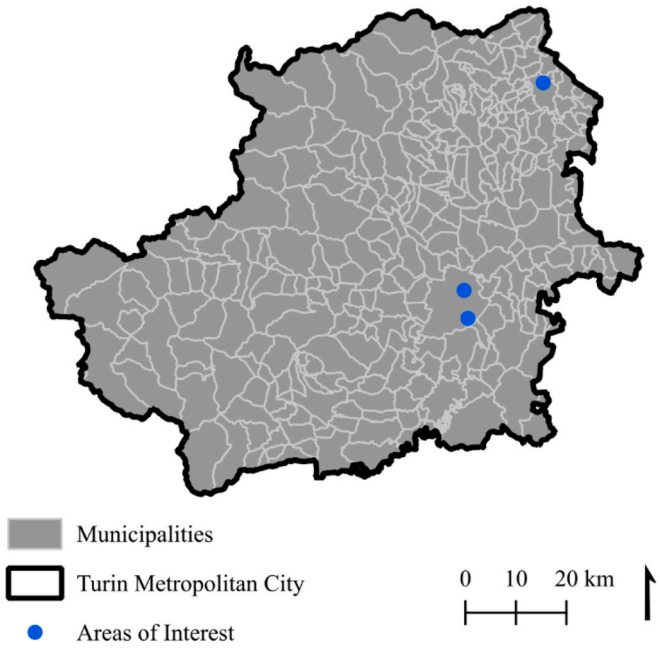


Fig. 1. Localisation of the three AoIs in Turin Metropolitan City.

one hand, it resulted in the need to meet the pressing housing demand through intensive poor-quality buildings, especially in peripheral areas as *Barriera di Milano* (AoI1). In this case, high-rise buildings were the prevalent building type. On the other hand, dispersed urban development took place on the hill (AoI2), with new houses realised for the upper classes.

The third case study (AoI3) is located in the San Lorenzo district, in the Eastern part of Ivrea, a small city at the foot of the Alps. San Lorenzo has been identified as one of the pilot areas for the realisation of a Renewable Energy Community, as it mixes different urban conditions and morphologies, thus making it an ideal case study for analysing the productivity in complex *peri*-urban environments.

3.2. Data acquisition

The first phase of the research entails the creation of a supporting dataset for carrying out the assigned tasks within the QGIS and ArcGIS software. GIS-based model investigations necessitate access to environmental and geographic data relevant to the selected study area, so this endeavour requires identifying and collecting the specified datasets and parameters, ensuring their alignment with the precise specifications and requirements to execute the planned analyses and computations within each software environment. Therefore, a preliminary phase consists of the definition of the parameters required by the two software tools for solar radiation.

3.2.1. Tools requirements

Both tools require a Digital Elevation Model (DEM) and two derived products (slope and aspect) as key geographic parameters. The r.sun tool, part of GRASS GIS – Geographic Resources Analysis Support System –, provided in QGIS requires the elevation layer separately from the ones returning slope and aspect of every cell, while Raster Solar Radiation (RSR) allows the user to choose whether to submit them or not (thus making the tool compute them). Because of this, RSR, released in November 2023 as part of the updated spatial analyst in ArcGIS Pro 3.2, shows faster elaboration time compared to its previous version, the Area Solar Radiation tool, which calculated slope and aspect at every iteration [39].

As for the other geographic parameters, the two tools differ. While r.sun allows the user to optionally insert a raster file with latitude values



Fig. 2. Areas of Interest (from left to right: AoI1: urban area in Barriera di Milano; AoI2: sparse settlement on the hill of Turin and AoI3: peri-urban area in Ivrea).

reported in each cell, RSR automatically computes it from the input elevation model. QGIS also considers the possibility of having a horizon information map, while ArcGIS computes it from the DEM, with only the possibility to modify the vertical scale of the DEM itself – enhancing or reducing the impact of the casted shadows. For this study, none of these options was considered.

In ArcGIS Pro, users can choose between generating a single total insolation value for the full period or discrete radiation values for each defined interval. This study utilises the former method. As for the time interval, r.sun computes only the daily radiation, while both ArcGIS tools (ASR and RSR) make it possible to modify the calculation time span from less than one hour to one year.

As part of the radiation parameters, ArcGIS requires the user to define the diffuse model type, diffuse proportion and transmittivity. The first of them can be set to be "uniform overcast sky" or "standard overcast sky", with the latter – adopted in this study – having a variation in the incoming diffuse radiation flux according to the zenith angle. The share of direct (or beam) and diffuse radiation is an additional parameter to be collected: it is inputted through a single number in RSR, as a raster file in r.sun. Moreover, QGIS allows the estimation of the reflected radiation, too, thanks to the possibility of inputting a raster file that returns the albedo values. This option was not used in this study. Finally, to quantify the atmospheric transparency r.sun requires the Linke turbidity factor T_L as a raster file, while RSR requires the transmittivity, which is computed based on the T_L.

An overview of the inputs, with their nature and the data type, is returned in Table 1.

3.2.2. Required parameters

Based on the tools requirements, the input parameters to be defined by the user are the elevation layer, Linke turbidity factor, and the Diffuse-to-Global radiation ratio (DG).

Considering the need to have high accuracy in the reconstruction of the surfaces of the urban fabric, this study used Digital Surface Models (DSMs) for extracting the elevation information. In particular, there is the need to use DSMs with 50 cm Ground Sampling Distance, respecting the requirements set by Kausika et al. [21], who claim that 50 cm is the minimum spatial resolution to model irradiation on rooftops. Coarser resolutions can be used for block – 5 m – or regional levels – 30 m.

Table 1
Input parameters for QGIS r.sun and ArcGIS Pro RSR.

Input	QGIS (r.sun)		ArcGIS Pro (RSR)	
	Nature	Type	Nature	Type
Digital Elevation Model	Required	Raster	Required	Raster
Slope and aspect	Required	Raster	Optional	Raster
Latitude	Optional	Raster	Computed	
Horizon	Optional	Raster	Computed	
Diffuse model type	n.a.		Required	Text
Diffuse radiation	Optional	Raster	Required	Number
Reflected radiation	Optional	Raster	n.a.	
Turbidity	Optional	Raster	n.a.	
Transmittivity	n.a.		Required	Number

The Linke turbidity factor, $T_{L,}$ has been defined by Eltbaakh et al. [40] as the factor returning the number of clean dry atmospheres necessary to equal the attenuation effect of the extraterrestrial radiation of the real atmosphere. Therefore, this is a good indicator to assess the effect of aerosols [41] and water vapour [42]. Moreover, it is particularly helpful when using algorithms such as RSR and r.sun, as it corrects the biases derived from the clear-sky radiation model used. According to Page [43], it is a function of the air mass, the observed irradiance normal to the solar beam, the solar constant and the *s* factor – defined as the reduction factor for mean solar distance at a specific time.

As previously mentioned, RSR requires transmittivity *T*, which was computed, starting from the Linke turbidity factor, according to Equation (1):

$$T = \exp\left(- 0.8662 * T_L * m * \frac{1}{9.38076 * m} \right) \# \quad (1)$$

where m is the air mass, −0.8662 is a standard calibration coefficient for the T_L [44] and $(9.38076*\mathrm{m})^{-1}$ represents the Rayleigh optical depth based on Kasten [45]. In order to use interrelated inputs, thus maximising the comparability between the elaborations with the two tools, Equation (1) was used to compute transmittivity from the gathered turbidity factors.

The global horizontal radiation is the result of three main components – direct, diffuse and reflected radiation. Measured in $\mathrm{kWh/m^2}$, it quantifies the power of solar energy striking the Earth's surface. The relevance of the diffuse component is quantified by the diffuse ratio, a parameter ranging from 0 – when the whole of solar radiation is direct – to 1 – in the absence of beam radiation. This amount of global irradiation is scattered in the atmosphere, with a sequence of micro-reflections caused by water vapours – in the form of suspended water and clouds – and other particles – such as PM2.5, pollutants and other components of the smog, particularly relevant in urban areas.

3.2.3. Data sources

Based on the review by Anselmo and Ferrara [12], this study collected the necessary weather parameters from widely used open data sources in order to provide a reliable dataset. In particular, it was decided to use datasets published both by public agencies and private firms. As for the former, data from the Joint Research Centre of the European Commission (made available through PVGIS, Photovoltaic Geographical Information System) and ENEA (Italian National Agency for New Technologies, Energy and Sustainable Development) were gathered, while for the latter data from SoDa (Solar radiation Data) website, QGIS support documentation [46], and Metenorm software

(v8.2.0) were used. Historical time series were built with temporal data coverage depending on the sources, defining for each source single monthly values, calculated as the average of the values of all the considered years.

PVGIS, with its most recent solar radiation database SARAH-3, is a web GIS elaborated by the European Commission which provides data on solar radiation and potential PV production for any location on Earth, except for the North and South Poles, in a time range from 2005 to 2023. The other available dataset is the ERA5 – which reanalyses datasets from the European Centre for Medium-Range Weather Forecasts –, providing climate variables and irradiance values in uncovered areas. Validation against ground station data, from 2005 to 2023, provides acceptable error margins [47]. The spatial resolution of SARAH-3 is at 0.05° x 0.05°, whereas ERA5 is coarser at 0.25° x 0.25°. Data are provided in different aggregations, from hourly data up to the whole year, in the form of the Typical Meteorological Year (TMY). For this research, both monthly data and the TMY were used to extract the Diffuse-to-Global radiation ratio. As for the former, average monthly values have been calculated considering the whole SARAH-3 data coverage (2005–2023), the same period used for the realisation of the TMY.

ENEA returns yearly data on 243 Italian municipalities, estimated from satellite data. Extra terrestrial radiation is processed through the model by Bourges, Sacré and Caubet (1984). Global horizontal, direct normal and diffuse horizontal radiation data are returned in separate tables, with each value being an average of the time period 2006–2022. Global horizontal and diffuse horizontal radiation values were extracted to compute the DG.

SoDa offers various services encompassing solar, meteorological, altitude, astronomical, and atmospheric data. Specifically, it provides solar radiation and meteorological data services for solar photovoltaic and thermal site assessment, electricity production monitoring, forecasting, and spectral radiation services [48]. Solar radiation data are provided both as tables for specific locations and in maps with a Ground Sampling Distance equal to 1°. Maps are derived from the Copernicus Atmosphere Monitoring Service, with monthly averages of the time period 2005–2020. Based on this source, both T_L and DG information was derived.

Meteonorm software provides a comprehensive climatological database for solar energy applications, offering stochastically generated typical years based on long-term monthly means for global locations, serving as a standardisation tool and data source for engineering design programs, environmental research, agriculture, forestry, and other meteorological and solar energy-related endeavours, with ongoing time-series data sourced from satellites and reanalysis data. This software allows specifying the dataset and period for calculations. The "contemporary dataset", the dataset used in this research, covers the years 2000 to 2019 for air temperature, dew point temperature, wind speed, wind direction, days with precipitation, and precipitation amount, while radiation data is available from 2001 to 2020 [45]. Also in this case, both T_L and DG values vere gathered.

Finally, the GRASS GIS manual for r.sun [45] provides reference values – aggregated in four categories, namely mountains, rural, city and industrial – for the Linke turbidity factor. These are set to be valid in a mild climate in the northern hemisphere.

As for the DSM, it was decided to use DSMs resulting from the LiDAR acquisitions of the TerraItaly™ Metro HD (in Turin) and DT4Energy.com (in Ivrea) projects, both carried out by Compagnia Generale Ripreseaeree S.p.A. with a Leica CityMapper-2 digital sensor. These elevation layers were realised for the SDG11 Lab, where the research has been carried out. The LiDAR operates on a wavelength equal to 1.064 mm, acquiring on average 40 points/m^2. From the classified LiDAR point cloud, three-dimensional shapefiles of the roof pitches have been extracted, as shown in Fig. 3. All solar radiation values are referred to the pitches as the minimum units of analysis.

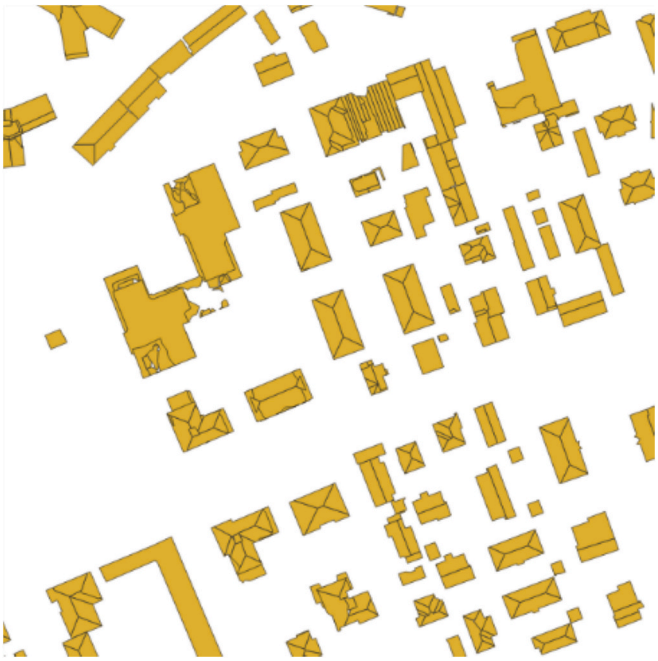


Fig. 3. Example of roof pitches shape.

3.3. Test matrix

Once the necessary inputs have been obtained, the second phase involves calculating solar radiation using ArcGIS Pro RSR and QGIS r.sun. These clear-sky models estimate insolation based on solar geometry and Digital Elevation Models, generating raster datasets where each pixel represents the total solar radiation received over the specified time periodAfter data gathering, the second phase consists of the actual elaboration of the solar radiation, to be later translated into the PV potential.

A total of five different values for the T_L and six values for the DG were gathered for each month. The first test, to be used as a reference, uses the average values of both parameters. Then, both parameters are maximised and minimised. Finally, the impact of the variation of a single parameter is explored by comparing the minimum, average and maximum while keeping the other parameter stable at its average. Each test is coded according to the value (min, avg and max for minimum, average and maximum) of the parameter, with T being the Linke turbidity factor and DG being the Diffuse-to-Global radiation ratio. For example, TavgDGavg stands for the test with average values of both T_L and DG.

The operational workflow of the two tools differs: while RSR allows for the computation of aggregate monthly radiation, r.sun requires the selection of a representative day for each month. Once the tool is run for the average days (typically the 15th or 16th of each month, as defined by Klein [49]) – representative of the solar geometry throughout the month –, the obtained radiation value is multiplied by the number of days in the corresponding month to determine the total monthly solar radiation. Finally, for both tools yearly radiation is calculated as the sum of monthly radiation values. The list of representative days, extracted from Klein [49], is outlined in Table 2, alongside the monthly day count.

On the contrary, RSR makes it possible to define the time interval according to a start and an end date. For this research, the monthly periods in the year 2024 were used. In this way, it is necessary to aggregate values only to produce the yearly sum.

3.4. Computational workflow

Both QGIS and ArcGIS tools return raster files as outputs, each coded

Table 2
Day number and number of days for each month of the year.

	January	February	March	April	May	June	July	August	September	October	November	December
Representative day	17	47	75	105	135	162	198	228	258	288	318	344
Number of days	31	28	31	30	31	30	31	31	30	31	30	31

with the AoI, the code of the test, and the month they refer to. These raster files are processed with a Python routine developed by the authors[1] which, using mainly the libraries Geopandas and Rasterio, returns a separate layer with the monthly and yearly photovoltaic potential. All analyses are performed at a disaggregate level on roofs.

The Python script loads and reprojects both vectors (roofs and buildings) and rasters (the outputs of the final radiation), before performing zonal statistics, i.e., to calculate the median of pixel values contained in each geometry. Then, the monthly PV potential is calculated based on Equation (2), described in [12] as the most used in literature:

$$E = I^{*}\eta^{*}PR^{*}A\# \quad (2)$$

where

- E is the electricity output;
- I is the solar radiation (the median value calculated through zonal statistics)
- η is the conversion efficiency of the panel, that is the share of solar energy converted into produced electricity, quantified according to [37] to be 26 % (with a ± 0.3 % range not considered in this study);
- PR is the Performance Ratio, expressing the efficiency of the support system, assumed to be 85 %;
- A is the exploitable area, calculated as 25 % of the useful pitch surface based on the total surface, after excluding a 1 m inner buffer, to be used for installation and maintenance).

This process is repeated for each AoI and test, returning geospatial data with monthly and aggregate yearly PV potential. The comparison between tests is carried out by analysing not only the numerical values, but also the principal trends which emerge by plotting the results in graphs. Specific attention is to be devoted to the relative differences among the outcomes of the two tools and the correlation between the input parameters and the outcomes.

A synthesis of the workflow, from data collection (paragraph 3.2.3) to the definition of the photovoltaic potential, is presented in Fig. 4.

3.5. Validation

The fourteen tests are validated against four tests carried out in PVGIS: two calculating the monthly radiation for each roof pitch, and calculating the photovoltaic potential according to Equation (2), two obtaining the yearly photovoltaic yield directly. These tests are carried out both by using accurate roof geometries (with slope and aspect calculated based on the high-resolution Digital Surface Model) and with standard geometry. The parameters for standard roof geometry – specifically 20° slope and South-facing orientation – were defined based on those adopted for the Digital Building Stock Model [50]. In this way, it is also possible to observe the impact of accuracy in roof geometry modelling for the photovoltaic potential estimation.

While PVGIS is not casting shadows from neighbouring buildings, the accuracy of this tool is widely acknowledged in the literature. For this reason, it was decided to use it as a source for the validation dataset. The first two tests are meant to observe the overall accuracy of solar radiation modelling. Indeed, they use the same Equation (2) that is used for calculating the PV potential according to both r.sun and RSR, with the only element which varies being solar radiation. The other two tests verify the formula itself: while Equation (2) is the most used in literature when calculating GIS-based solar potential [12], PVGIS power performance model calculation takes into account the additional parameters of operating temperature and wind speed [47].

The two principal metrics to validate results are the Mean Absolute Error (MAE) and the Root Mean Square Error (RMSE). The combined use of these metrics allows for a comprehensive error analysis: the former reflects the overall accuracy, while the gap between the two serves as an indicator of the variance in the error distribution, revealing potential systematic inconsistencies in specific urban geometries.

4. Results

This section presents the findings as divided into three main categories. First, the results of data gathering for the definition of the input dataset for the calculation of solar radiation are presented. Then, QGIS and ArcGIS outcomes – respectively – are presented, highlighting the principal variations and trends which can be observed. Finally, the correlation between weather inputs and the outcome is explored.

4.1. Input parameters summary

4.1.1. Roof slope and orientation

The slope and aspect parameters are computed, respectively, through the homonym tools in QGIS and ArcGIS Pro, returning the same results. Both tools – included in the raster analysis section – require as only input the DSM and return the inclination and orientation as angles, using degrees as units of measure. Considering that the slope and orientation of the roof are essential for solar irradiation calculations, obtaining this data from DSM files enhances the accuracy of energy efficiency assessments and architectural analyses.

The average roof slope is the highest in AoI1 (39.28°) and lowest in AoI3 (33.33°). Nevertheless, in AoI2, there is the highest share of pitches that can be considered flat (6.53 % with a slope lower than 10°). Optimal tilt angles of 40°, 39°, and 41° were identified for the three AoIs using the PVGIS tool [47]. This similarity reflect close latitudinal positions (45.095°N, 45.045°N and 45.470°N for the three AoIs). The three AoIs have a similar share of pitches comprised in a ± 10° range from the optimal slope, with the maximum in the hill of Turin (38.3 %) and the minimum (Ivrea case study) being 33.2 %.

As for the aspect, the urban structure of the three districts is very differentiated. First, AoI1 is mostly flat, with height differences comprised within a 60 m range. Without terrain constraints, buildings are organised in two ways: in the South-Western part, they evolved organically, while in the remaining area, they were built in splints, with a homogeneous structure. The considered portion of the hill is built on a North-East-facing slope, and it is characterised by a general prevalence of roads built on the maximum slope. Buildings are organised along the road, following the slope of the hill. Finally, in Ivrea, there is a South-facing slope, with roads and buildings located along the contour lines. From this it derives a wide presence of South-facing pitches. According to PVGIS [47], the optimal orientation is South-facing in all three areas, with differences comprised within a ± 1° range. The highest share of optimum-oriented pitches can be observed in Ivrea (9.5 %), three times larger than in Barriera (3.7 %).

[1] Available at https://github.com/anselmoseb/PV_AccuracyAssessment.

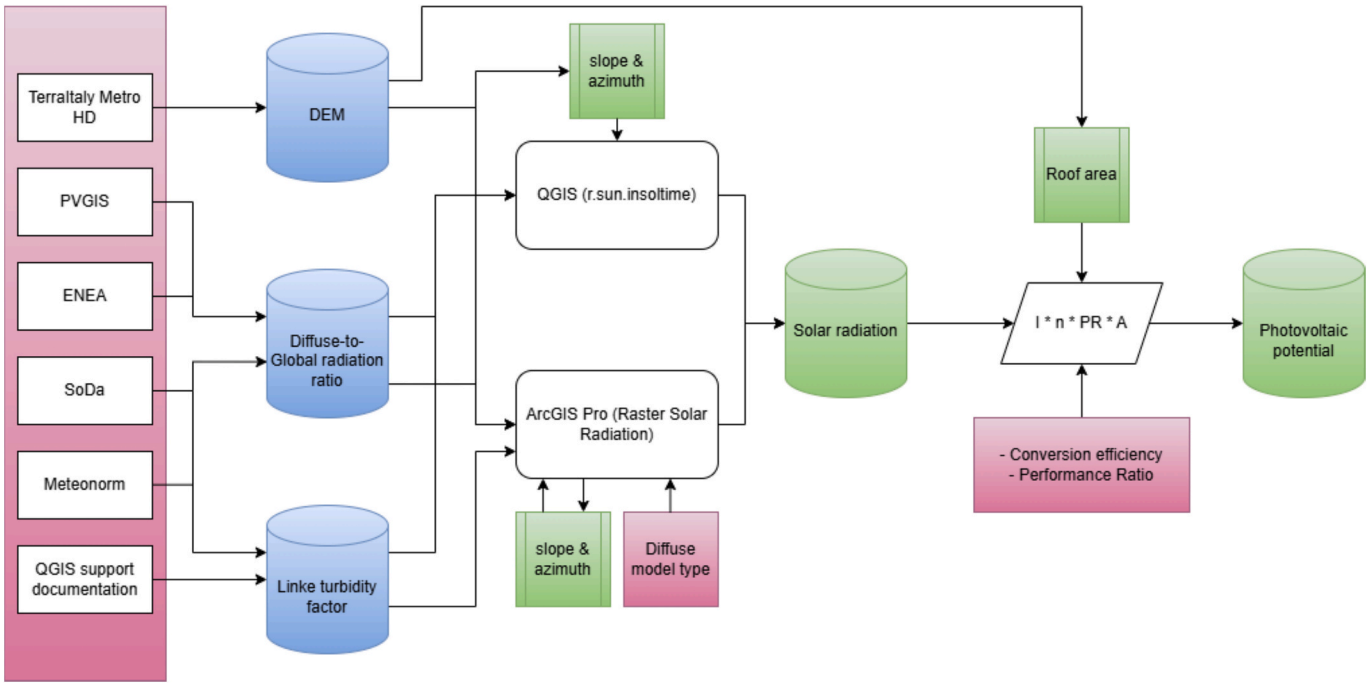


Fig. 4. Schematic representation of the presented workflow.

4.1.2. Diffuse-to-Global radiation ratio

The Diffuse-to-Global radiation ratio (DG) represents the proportion of total ground-level radiation attributed to the scattered component. The DG values are collected from PVGIS (from both the monthly radiation calculator and the TMY), Meteonorm, SoDa and ENEA. PVGIS utilises an anisotropic two-component estimation model presented by Muneer [51], while Meteonorm estimates the diffuse component based on the models of Perez et al. [52] and Ridley et al. [53]. SoDa provides data from both the Meteosat constellation, in the form of tables, and the Copernicus Atmosphere Monitoring Service, in the form of raster data. Finally, ENEA published irradiation data for 243 localities in Italy, based on weather stations information: for this study, values from Turin have been used for AoIs 1 and 2, while for Ivrea, an average between the values of Turin and Biella (equidistant from the AoI) has been used as input.

No relevant discrepancies can be observed between the three AoIs, with monthly averages comprised within a 3.7 % range. The maximum differences can be observed in the PVGIS TMY, 11.2 % on average, with a peak of 21.4 % difference between the values observed in March in AoIs 1 (65.9 %) and 3 (44.5 %). On the contrary, the minimum discrepancies can be observed in the ENEA dataset, where there is perfect correspondence between the shares of DG registered in May.

Fig. 5 plots the variations of the monthly DG values, including the average values together with the curves of the different sources, for AoI3 (Ivrea). The peak can be observed in October (55.3 % on average), with PVGIS TMY returning the highest value (79 %). In general, DG values are maximised in spring and autumn, with the lowest values in summer.

Most sources show comparable trends in the form of a generally flat curve, with a first decrease of the diffuse radiation in March, followed by an increase for one or two months and a general stabilisation during summer, before a second increase in autumn. The most notable exception is represented by PVGIS TMY values, which have the highest fluctuations with visible peaks in February, May, July and October. On average, PVGIS TMY and SoDa tables values are the highest (55.6 % and 55.4 % on average throughout the whole year), contrary to the PVGIS monthly values, which are the lowest (38.1 %).

4.1.3. Linke turbidity factor and transmittivity

Linke turbidity factor data were gathered from SoDa and Meteonorm. In the SoDa dataset –monthly raster files with Linke with 0.8°

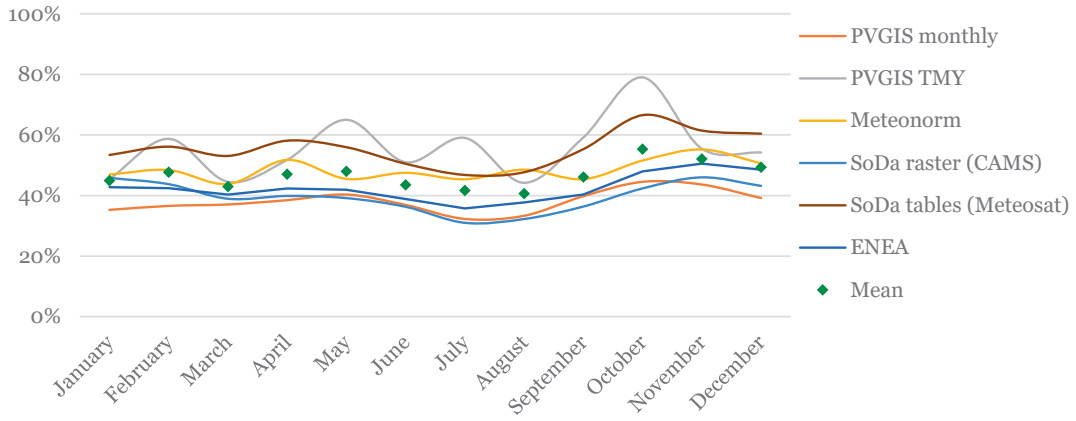


Fig. 5. Diffuse-to-Global radiation ratio trends in AoI3 (Ivrea).

resolution –, the Linke turbidity factor is calculated by integrating global satellite data on clear sky radiation, precipitable water vapour, and aerosol optical depth with ground-level measurements of turbidity, using fusion methods to account for differences in spatial resolution alongside water vapour maps and orography information [54]. On the other hand, Meteonom determines Linke turbidity by using satellite data and ground station measurements. For both Turin and Ivrea, the closest Aeronet ground station is located in Ispra (VA, Italy), around 110 km away. Two configuration options are available in Meteonorm, with the turbidity factor being returned from the closest ground station and interpolated data for a given point [55].

Additional T_L values derive from the documentation supporting the use of the r.sun tool, provided by Hofierka et al. [46]. These values are aggregated into broad categories – city, mountains, countryside and industrial areas – and are intended to represent average values for a mild climate in the northern hemisphere. As the AoI3 has hybrid characteristics – being a *peri*-urban area inside a rural region – it was decided to consider both urban and rural values, while the other two case studies were considered as fully urban.

Discrepancies between the three AoIs can be observed only in the Meteonorm interpolated and SoDa datasets. However, in both cases, these are very limited, on average 0.09 for the former and 0.18 for the latter. While the minimum difference can be observed in January and December for the Meteonorm interpolated dataset (0.07), the highest is observed in May and June according to SoDa (0.3).

Fig. 6 shows variations in monthly T_L values, including the average values together with the curves of the different sources, for AoI3 (Ivrea). On average, it can be observed that starting from January, Linke values show a slight increase, reaching a peak in June (4.24 on average) before descending towards the end of the year in December. However, different sources follow slightly different patterns. While most sources have a peak in either June or July, Meteonorm interpolated anticipates it to April. While a complete analysis of climatological time series falls out of the scope of the paper, it is worth citing that, given he global models employed by Meteonorm, this is likely due to an overestimation of combined impact of background aerosols and spring circulation [55]. On the contrary, all sources have their minimum in winter, be it January or December. Moreover, while Meteonorm interpolated and both QGIS values have a constant increase until the peak, followed by a decrease, SoDa and Meteonorm Aeronet have a second peak in October, with a sharper decrease towards December.

Transmittivity values are inversely proportional to the Linke turbidity factor, with the maximum values in winter and the minimum in summer.

4.2. Estimated photovoltaic potential

According to the different configurations, a set of 7 calculations (see Table 3) was planned to understand both the output variability range and the impact that input parameters have on the outcomes. For all calculations, the same PR, panel efficiency and exploitable area are taken into account. As each calculation is carried out both in QGIS and ArcGIS Pro, 14 outcomes are expected in total. Table 3 describes the alternative input configurations for the seven tests, carried out in both QGIS and ArcGIS Pro.

As mentioned in paragraph 2.1.1, r.sun returns only daily radiation, while RSR can compute radiation in a user-defined span of time. However, the design modeller embedded in QGIS allows the automation of part of the process (the creation of rasters from numerical values of T_L and DG, the calculation of slope and aspect, and the calculation of solar radiation in representative days for the whole year), while in ArcGIS, the process is carried out for each month separately. Beyond the time required to define the inputs singularly, ArcGIS proved to be slower also in the processing time, with a total of 10 h, against the four hours of QGIS. Indeed, while the 12 elaborations of representative days for a single year take about 680 s in QGIS, ArcGIS requires 1715 s on a regular desktop PC. Fig. 7 shows the resulting monthly radiation according to ArcGIS RSR and QGIS r.sun tools (plan TavgDGavg) for AoI1 in August, to be referred to single pitches and used as the basis for calculating the PV potential.

The analysis of the PV potential for every pitch is done by running a Python script, which takes approximately 2 h for all the results and returns a geospatial layer for each test – with roof geometries enriched with monthly and yearly radiation – and a single final file including yearly radiation according to all tests.

4.2.1. R.sun results

First, the results of the r.sun tool are observed. Fig. 8 returns the boxplots of the photovoltaic production per roof across the three AoIs, given that the average roof dimension is 42 m^2, 23 m^2 and 49 m^2 for the three AoIs, respectively.

It clearly emerges that the production is maximised in Aoi3, while the minimum values can be observed in AoI2. According to the plan averaging both parameters (TavgDGavg), the median values of the monthly production are 913.4 kWh, 393.5 kWh, and 1046.8 kWh for the three AoIs. From this, it can be assumed that the South-facing slope that characterises the AoI located in Ivrea is positively affecting the photovoltaic potential. Moreover, the building density of AoI3 is limited, with 14.7 % of buildings with respect to the AoI surface. AoI1 is generally flat, with a higher building density (21.1 %), resulting in significantly lower values. Finally, AoI2, despite its low density (4.6 %), is affected by the lowest values due to the unfavourable hill slope.

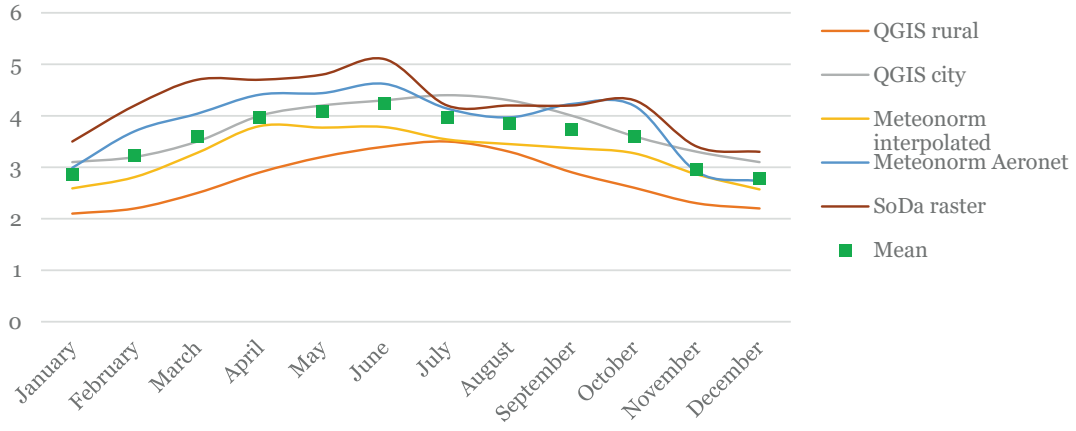


Fig. 6. Linke turbidity factor trends in AoI3 (Ivrea).

Table 3
Planning of the tests.

	TavgDGavg	TminDGmin	TmaxDGmax	TminDGavg	TmaxDGavg	TavgDGmin	TavgDGmax
Linke turbidity factor	avg	min	max	min	max	avg	avg
Diffuse-to-Global radiation ratio	avg	min	max	avg	avg	min	max

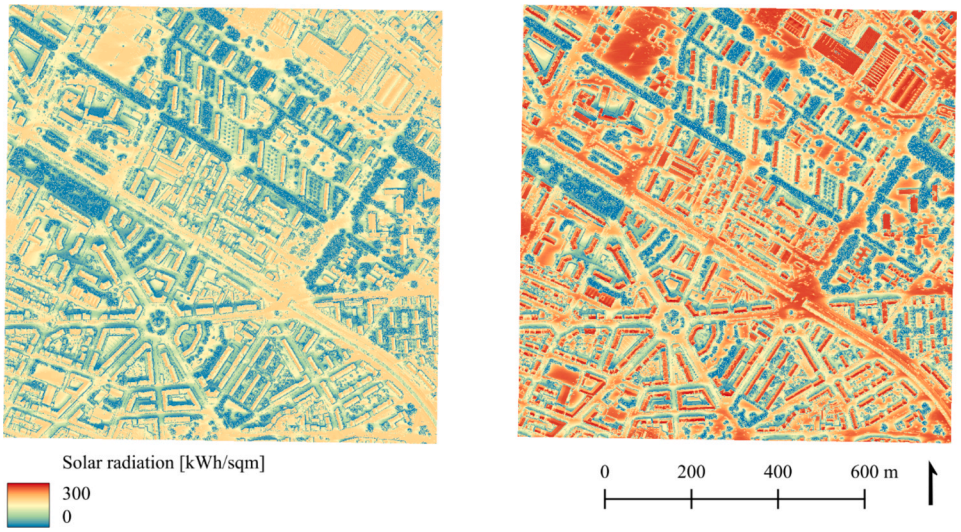


Fig. 7. Monthly radiation in August according to r.sun (left) and RSR (right) in AoI1.

Key differences can also be observed when looking at the discrepancies between the tests. Fluctuations in the total production are comprised in a ± 1 GWh difference from the TavgDGavg value across the three AoIs. Turbidity has the strongest influence, with minimum production deriving from the maximum T_L values and the maximum from the minimum T_L values. On the contrary, there is no clear correlation between DG values and productivity. With constant T_L, lower DG leads to lower production values, but the same impact on production values cannot be observed when varying the turbidity.

As for the differences between the tests in the three AoIs, in absolute values, these are maximised with the highest production values. Nevertheless, despite the absolute differences, the percentage differences remain constant across the two AoIs located in Turin, ranging between −3.5 % and + 4.9 %. On the other hand, in Ivrea, discrepancies are significantly higher, ranging between −5.9 % and 8.2 %.

4.2.2. *Raster solar radiation results*

Results of the RSR tool follow, plotted in Fig. 9, with the boxplots of the photovoltaic potential per roof across the three AoIs.

Similar trends to those observed for r.sun can be observed, with AoI3 showing the highest values, followed by AoIs 1 and 2, respectively. Indeed, median values of the plan inputting average parameters (TavgDGavg) are, for the three AoIs, 1482 kWh, 563.8 kWh and 1626.7 kWh. Therefore, also in this case, a favourable slope and building density are key drivers for higher photovoltaic production.

Discrepancies from the TavgDGavg test are comprised in a ± 7 GWh (28 %) range, when considering the three AoIs simultaneously. In this case, it is possible to observe a direct proportionality between DG and photovoltaic potential, while no clear correlations appear between T_L and PV production. Indeed, while it emerges that, with constant DG, the PV potential is 1.4 GWh higher with minimum turbidity (and therefore higher transmittivity), the same pattern cannot be observed across all the other tests.

When ordering tests according to the total production, a general homogeneity appears between the full dataset and the two AoIs located in Turin, while AoI3 shows different values. In particular, the test TmaxDGavg – with maximum turbidity and average Diffuse-to-Global radiation ratio – is considered among the most productive, while in the other AoIs it is ranked in the middle. In light of the general homogeneity, it can be stated that fluctuations are mostly dependent on the relation between roof geometries and DG. In Ivrea case study, with reduced impact of shadowing and favourable building orientation, an higher share of global radiation is direct compared to the other two AoIs. Therefore, this test represents an average, given the average input DG; on the contrary, in denser urban areas (AoI1) and places characterised by unfavourable orientations (AoI2) the share of DG on the global solar radiation is higher and even an average configuration leads to higher production. Differences between the three AoIs can be further observed when considering the ranges in which values are comprised. Compared to the TavgDGavg plan, mean differences are comprised in a ± 28.5 % range when observing the full dataset. In AoI1, the TavgDGavg test returns average values compared to the other tests, with a 31 % difference, which can be observed both in positive (compared to TavgDGmin) and negative terms (compared to TmaxDGmax). However, a clear imbalance appears in both AoI2 – with positive differences up to 63 %, compared to 16 % of negative differences – and AoI3 – with values comprised between −30.7 % and 18.8 %.

4.3. *Cross-tool comparison*

When comparing results from the two tools, the principal element which can be observed across all the tests is the fact that, on average across all tests, a single roof located in Ivrea has a higher production potential per square metre than those in Turin, and that AoI1 has higher values compared to AoI2. On average, across all tests and the two tools, compared to AoI1, AoI2 returns values 57 % lower, and AoI3 15 % higher. This trend is consistent throughout all tests, with some notable exceptions. First, there is one case – TavgDGmin according to RSR – where the production in Ivrea is lower than the Turin production (−0.14 % difference). A similar trend, with lower magnitude, can also be observed according to r.sun, with the positive difference between Ivrea and Turin reduced to 11.1 %. On the contrary, for plan TmaxDGmax, it is

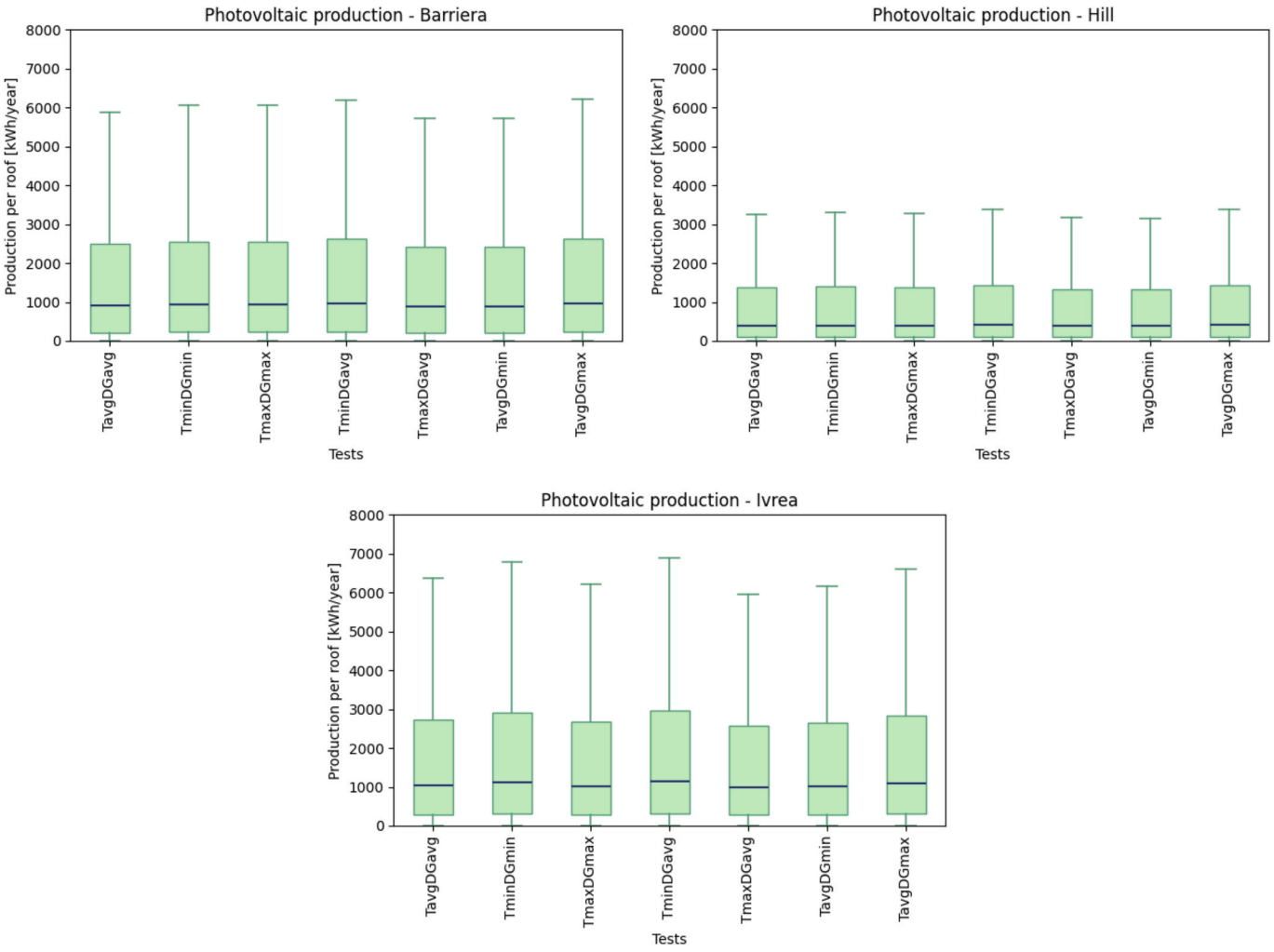


Fig. 8. Boxplots on the Photovoltaic production across the three AoIs (AoIs 1 to 3 from left to right) according to r.sun.

possible to note a sharp increase in the difference between AoIs 3 and 1 (42.5 %) according to RSR, while r.sun value remains below the average (11.4 % difference).

QGIS values are consistently lower than those returned by ArcGIS, with the average ratio between the former and the latter being 0.69. This value shows high fluctuations, with the ratio comprised in a range between 0.17 and 1.16. The highest discrepancy (ratio higher than 1) can be observed for the tests with T_L maximised (TmaxDGmax for AoI1 and the full dataset, TmaxDGavg for AoIs 2 and 3), while the lowest are registered across all AoIs for test TavgDGmin. These differences derive from the different impacts that input parameters have on the outcome in the two tools. Indeed, while in r.sun, turbidity is the major driver determining the magnitude of the PV potential, according to RSR, there is a major correlation between DG values and PV production. This results in high differences in the ranking of tests, especially for TminDGmin – among the least productive according to ArcGIS and the most productive for QGIS – and TmaxDGavg – the least productive according to r.sun and second-best according to RSR.

Based on the outputs of this phase, it is possible to derive the test with the closest values to the average and the output variability. While according to r.sun the use of averaged input parameters leads to average solar radiation – thus selecting TavgDGavg as the reference, with a 0.15 GWh difference from the average of all tests –, for RSR it is TmaxDGavg which minimises the discrepancy from the average, 0.48 GWh. Moreover, QGIS results are closer to the average – with maximum discrepancies being − 0.72 GWh and + 1 GWh – compared to those returned by ArcGIS – comprised in a − 8.7 GWh, + 4.47 GWh range.

Once the reference test has been chosen for each tool, it is possible to refine the temporal resolution and analyse monthly trends. Fig. 10 shows the monthly PV production according to the two reference tests, with whiskers showing the upper and lower production boundaries.

First, it can be observed that throughout the whole year, ArcGIS values are significantly higher compared to those returned by QGIS. The month with the highest difference is October, when QGIS values are equal to 0.36 of ArcGIS ones, while in June the ratio between QGIS and ArcGIS is 0.7. Second, QGIS range is highly limited compared to that of ArcGIS, with absolute discrepancies being on average 72 MWh/year for the former and 560 MWh/year for the latter. Finally, QGIS production trends are more linear, with a gradual increase from January to July – with the peak being 2.1 GWh according to the average test –, followed by a decrease until the yearly minimum in December. The only exception is given by the upper PV production limit, with the production being maximised in June (2.2 GWh). ArcGIS production trends see a sharper increase in the first part of the year, with the peak which can be observed in May – 3.5 GWh according to the average test –, followed by alternate decreases and increases, with minor peaks in July and October.

The observed monthly trends appear unsurprising, as they are similar to those observed for the input parameters. Indeed, as the Linke turbidity factor has a generally flat curve – with a gradual increase while moving from winter to summer –, also QGIS results show comparable trends. Moreover, the principal discrepancy from the trend can be

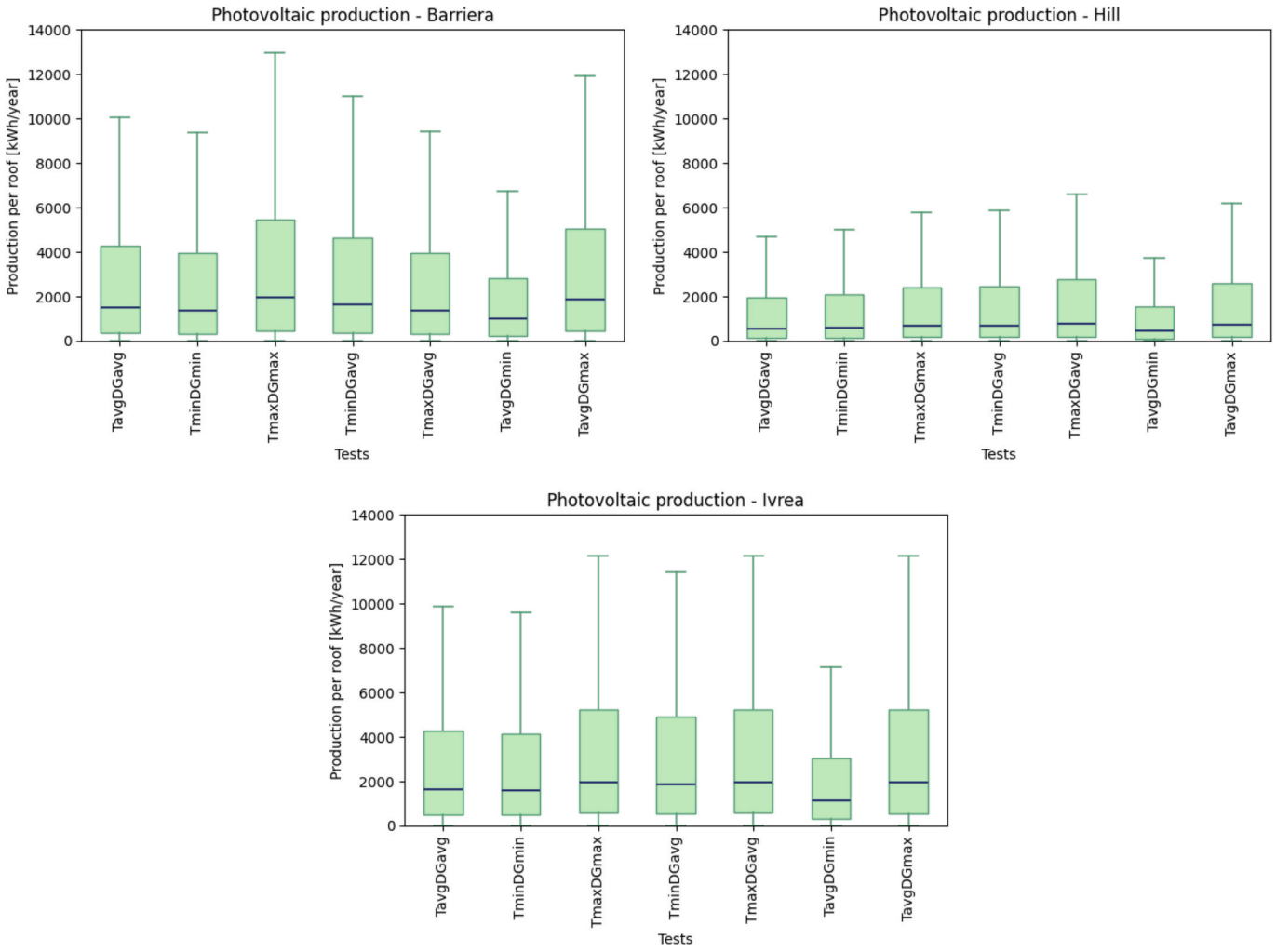


Fig. 9. Boxplots on the Photovoltaic production across the three AoIs (AoIs 1 to 3 from left to right) according to RSR.

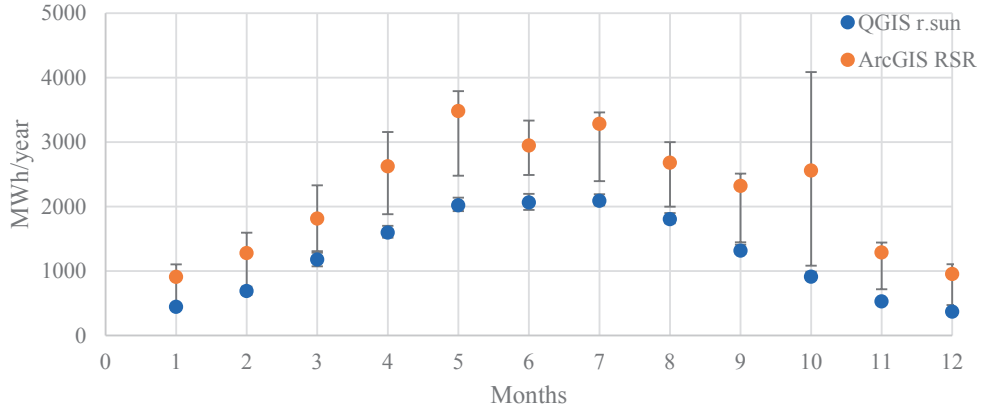


Fig. 10. Monthly PV production according to QGIS and ArcGIS.

observed in June, where turbidity is maximised according to SoDa raster, and the same peak can be observed in the production according to QGIS. Conversely, ArcGIS Pro monthly results are correlated with DG trends, with local peaks in May, July and October. In particular, the maximum discrepancy can be observed in October, when PVGIS TMY returned a share of 79 %, compared to the minimum (SoDa CAMS) of 42 %.

4.4. *Validation outcomes*

Validation is twofold. First, it observes the disaggregated monthly productivity with the use of the same Equation (2) being used for the results in the previous paragraph; second, it considers the yearly productivity based on the PVGIS power performance model.

4.4.1. Monthly results validation

Fig. 11 returns monthly validation results according to PVGIS. Areas return the range in which ArcGIS and QGIS values are comprised (MinMax in the legend), while rhombuses indicate the monthly production according to the test chosen as average (Avg in the legend). Finally, the lines indicate the monthly production trends according to PVGIS tests (with accurate roof geometries, acc in the legend, and with standard slope and orientation, std in the legend).

First, a systematic overestimation emerges when observing ArcGIS results, with this further enhanced by the fact that PVGIS does not include the cast of shadows, resulting therefore in higher theoretical estimates. On the contrary, QGIS returns values which are more aligned with PVGIS, in particular in terms of production trends. Indeed, both QGIS and PVGIS results show a gradual increase in production from January until the peak in July, followed by a constant decrease until the minimum in December, opposed to a more complex trend observable for ArcGIS. Nevertheless, some differences persist. Indeed, QGIS returns significantly lower values in winter months compared to PVGIS, while during summer it estimates a higher productivity. Across the three AoIs, the total yearly discrepancy is equal to 215 MWh and 650 MWh (with QGIS producing 15 GWh/year), observing differences compared to PVGIS results with accurate and standard roof orientation, respectively. ArcGIS discrepancies from the two tests are 11 GWh and 10 GWh (with ArcGIS producing 26 GWh/year). Moreover, when observing QGIS results, discrepancies are minimised during summer and early autumn, with differences from August to October lower than 45 MWh/month (based on an average production of 1.1 GWh/month). Using the PVGIS test with accurate roof geometries, QGIS returns a Mean Absolute Error (MAE) equal to 486 MWh and a Root Mean Square Error (RMSE) of 1.4 GWh, while for ArcGIS, the MAE is 1.719 GWh and the RMSE is 5.1 GWh. In both cases, the high discrepancy between MAE and RMSE indicates an inhomogeneous distribution of the error. A small percentage of roofs returns small errors, which strongly influence the RMSE.

Finally, it is possible to decompose the errors in the AoIs, as reported in Table 4. While the lowest errors can be consistently observed in AoI2, where the production is also minimum, the maximum errors can be observed in AoI1 when observing QGIS results, and in AoI3 when validating ArcGIS results. While the distribution of results derives from the magnitude of the PV production, making therefore unsurprising the lowest errors for AoI2, it is interesting to note that the validation results of the two tools differ.

QGIS values are generally closer to those of PVGIS, with the error mostly deriving from the shadowing. As AoI1 is characterised by a dense urban fabric, shadowing is impacting more results compared to AoI3. On the other hand, ArcGIS errors derive mostly from the magnitude of the results. As in AoI3, a higher productivity compared to the other AoIs was observed, from which it derives that ArcGIS errors are maximised in this area.

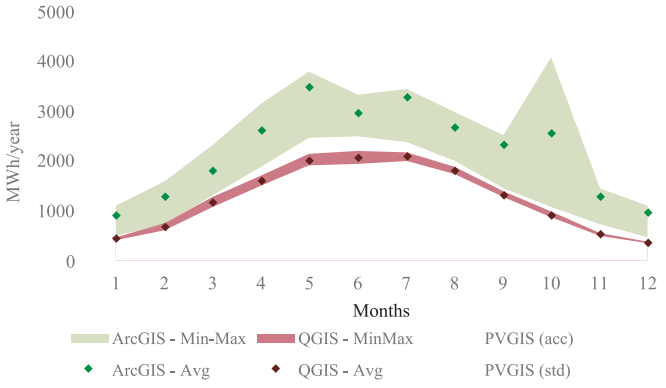


Fig. 11. Monthly radiation trends according to ArcGIS, QGIS and PVGIS across the three AoIs.

Table 4
MAE and RMSE values for the three AoIs.

			AoIs 1,2,3	AoI1	AoI2	AoI3
MAE	[MWh]	QGIS	486.04	630.49	288.82	405.95
		ArcGIS	1719.24	1472.96	1247.40	2213.87
RMSE		QGIS	1425.87	1854.20	592.00	1072.26
		ArcGIS	5136.85	5260.20	2629.29	5790.45

4.4.2. Yearly results validation

The second validation step aims to define the accuracy of the formula for estimating the PV potential (Equation (2) compared to the more complex PVGIS power performance model. Fig. 12 shows the boxplots for six tests: QGIS TavgDGavg and ArcGIS TmaxDGavg (the two tests returning average values for the two tools), the two tests using PVGIS monthly radiation calculation with accurate (PVGIS_MRacc) and standard (PVGIS_MRstd) roof geometries in combination with Equation (2), and the two tests using PVGIS power performance model with accurate (PVGIS_EYacc) and standard roof geometries (PVGIS_EYstd). This step is carried out by observing median and total production values for the whole year.

First, it emerges how all tests, with the exception of ArcGIS, show similar results, with all median values comprised in a 0.2 MWh ranges. ArcGIS median is 0.6 MWh higher than the average of the other medians. These discrepancies can also be observed when observing the percentiles, with significantly higher values returned by ArcGIS compared to the other tests. As for QGIS, while in the previous paragraph it was observed that it returns slightly lower values compared to those returned by applying Equation (2) to the PVGIS monthly radiation results, it emerges that, compared to both tests using the PVGIS power performance model, it slightly overestimates the PV potential. Indeed, while QGIS returns a median production value of 844.49 kWh and PVGIS monthly calculator 951.84 kWh and 952.63 kWh (for accurate and standard roof geometries, respectively), the two tests performed with the PVGIS power performance model return median values equal to 735 kWh and 900 kWh (for accurate and standard roof geometries, respectively). On average, the difference between results by the power performance model and Equation (2) is equal to −14 %. All median values, together with the total production across the three AoIs, are returned in Table 5.

The same trends observed for the median value apply to the total production, with all tests apart from ArcGIS comprised in a 3.7 GWh range and ArcGIS returning a total production 11.7 GWh higher than the average of the other medians. In the case of PVGIS power performance model tests, a significant discrepancy can be observed by comparing results given by accurate and standard roof geometries, with the former

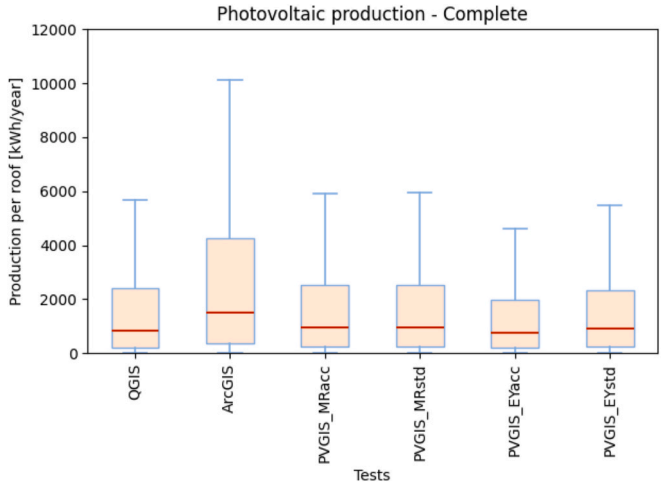


Fig. 12. Validation results for yearly production across the three AoIs.

Table 5
Median and total production values across the three AoIs according to the six tests.

	QGIS	ArcGIS	PVGIS – MR		PVGIS – PV	
	Acc	Acc	Acc	Std	Acc	Std
Median [kWh]	855.49	1482.80	951.84	952.63	735.00	900.00
Total [GWh]	14.98	26.12	15.20	15.63	12.01	14.05

being 15 % lower than the latter.

5. Discussion

From the previous chapter, it clearly emerges a systematic difference between results of r.sun and RSR, on both the magnitude of solar radiation and the principal drivers influencing results themselves.

The high sensitivity of r.sun to the Linke Turbidity Factor is rooted in its use of the European Solar Radiation Atlas (ESRA) model, where T_L is the core parameter for the definition of the optical thickness of the clear sky. It simultaneously modulates the decay of beam radiation and the intensity of scattering – which increases the DR. From this, it emerges an influence of T_L on DR too, with the former resulting more relevant. As r.sun computes radiation at discrete time steps based on solar geometry, any fluctuation in T_L recalibrates the entire atmospheric transparency. Moreover, as the attenuation law is exponential, even small variations in T_L produce relevant impacts. Conversely, RSR is based on the model by Fu and Rich [56], which prioritises the hemispherical sky-vault geometry over complex atmospheric physics. In this model, the diffuse fraction determines the weight of the sky-view factor. As a result, in urban environments – where complexity in roof geometry and self-shading are highly influencing – the autonomously modelled diffuse component becomes the critical factor in increasing solar radiation even in shaded areas, thus exerting a key influence on the total accumulated radiation compared to the more rigid beam component. On the contrary, transmissivity acts as a mere scaling factor applied to incoming radiation. From the comparison between the two tools, it clearly emerges the difference between a rigorous physical modelling of the atmosphere (r.sun) and a model primarily based on geometry (RSR).

As for the practical implications, it could be derived that r.sun.insoltime should be prioritised over RSR. As the latter “fills in” the shadows with scattered radiation, there is a general tendency to overestimate incident solar radiation and therefore PV potential. Nevertheless, given the high impact of the Linke turbidity factor on the results, accurate estimations of this input parameters are required. Moreover, r.sun allows for better computational efficiency through parallel processing. GRASS GIS leverages a spatial tiling strategy based on Python, which distributes the workload across CPU cores, while RSR uses its native parallel processing framework.

To contextualise the findings, it is essential to acknowledge the inherent limitations of the simulation. First, these are related to the temporal dimension. Indeed, the analysis uses historical time series for the definition of input parameters, while elaborations are based on a single year (2024). Performing the analysis on a wider time span would enable the consideration of the degradation of the panels, in order to better assess the trends in PV production across the years with different installation strategies. Moreover, the considered temporal resolutions are yearly and monthly. While this is appropriate for evaluating precision and accuracy of solar radiation tools, higher temporal resolutions are required for dimensioning a PV system in urban environments. Second, a default albedo value is considered, overlooking the variability in reflected radiation. Finally, shading is not considered in the PVGIS assessments. This would be made possible by the upload of a horizon profile, to be previously elaborated in a GIS environment.

6. Conclusions and future work

In conclusion, it is possible to point out the principal elements that emerged from this research in order to define possible future steps and provide guidelines for continuing the work, refining the results by increasing the precision and the temporal resolution. The goal of the research was to quantify the output variability between two alternative GIS tools for solar radiation estimation, testing alternative input configurations. 7 tests were carried out in both software, based on the alternative Diffuse-to-Global radiation ratio and Linke turbidity factor values.

First, from the comparison of the inputs required by the two analysed tools – QGIS r.sun and ArcGIS Raster Solar Radiation –, a general similarity emerges between them. The principal difference, which makes r.sun more suitable for large-scale assessments, is that r.sun accepts rasters as input for T_L and DG, thus enabling the possibility to better return the spatial variability. For example, in the case of extending the solar radiation analysis to the whole territory of the Metropolitan City of Turin, it would be necessary to render the differences between urban, rural and mountain areas, characterised by lower pollution and therefore less atmospheric turbidity. This point acquires even more relevance when increasing the scale of analysis, including broader and more heterogeneous territories. However, like r.sun, but differently from its previous version (Area Solar Radiation), RSR allows the user to input slope and orientation maps, resulting in shorter elaboration time and more efficient processes, as it is not necessary to compute them at every iteration. Moreover, it enables the setting of the diffuse model type, which can vary or not depending on the zenith angle. However, RSR does not imply the reflected component, with albedo values not being considered among the inputs. Finally, it is not possible anymore to set the viewshed algorithm by modifying sky size – or resolution –, zenith and azimuth divisions as it was allowed in Area Solar Radiation.

The two tools strongly differ in the outcomes, with ArcGIS returning values systematically higher compared to QGIS across the AoIs. First, the analysis was carried out on a yearly basis. The presented results showed different trends concerning the relation between input values and PV productivity, with QGIS r.sun results being correlated to T_L and ArcGIS Pro RSR results correlated to the DG. The same applies to monthly trends, with r.sun results following a linear trend – PV production increase in the first part of the year, peak in July and decrease in the second part of the year – and RSR a fragmented trend – characterised by peaks in June, May and October.

The variability of results based on alternative input configuration demonstrated that, despite the wide availability of weather data – returning both DG and T_L values –, the calibration of weather inputs is a crucial step to increase precision. Site-specific data, as the ones published by Fracastoro et al. [57] about the Linke turbidity factor, would remove an element of uncertainty from the calculation. Moreover, as both viewshed models provide comparable results in terms of spatial patterns, the possibility of using a single pyranometer to calibrate incoming solar radiation and adjust other values according to that emerges. On a wider scale, where it is not possible to install several pyranometers for the calibration, tools as PVGIS – returning solar radiation with high accuracy but not taking into account shadowing – can be used, identifying unshaded areas and defining correction factors in those areas.

For refining the results, two main elements can be taken into account. One belongs again to solar radiation, and it is about increasing the temporal resolution of the analysis. Indeed, only aggregated values were taken into account, observing the principal trends in cumulative productivity. Nevertheless, in order to understand how to fully unlock the photovoltaic potential estimation, a concept to be taken into account is the one of correlation, which stands for the temporal shift between the peaks in production and demand. Correlation is both seasonal – with higher demand during wintertime and peak production in summer – and daily because the energy needs are maximised during nighttime. For this

reason, further studies should look at the daily variations in productivity, even focusing on a single tool, selected based on this research. The second refinement deals with the calculation of the photovoltaic potential beyond the solar radiation analysis. More complex formulas already tested in literature – e.g., including the life cycle of the panel [38] or operational temperature and wind speed (as the PVGIS power performance model) – can be used.

Finally, additional studies along the lines of this research have the potential to study the precision of the results and claim what the reliability of both input datasets and tools is, but are unable to demonstrate the accuracy. For this reason, another research dealing with the validation of both inputs and results should be planned. Based on data and technology availability, it is possible to acquire a historical series from existing systems or to use a dedicated system. In both cases, it would be necessary to have a heterogeneous set of panels, able to model different shadowing and orientation conditions.

Initiatives like the EU Digital Building Stock Model (DBSM) aim to build a detailed solar cadaster at EU scale [50]. The gradual increase in data availability of the roof building morphology and higher-resolution digital surface models, should enable an increase in accuracy of the per-building solar estimates provided. Analysis like the one presented in this paper help assess the outcome provided at scale for smaller regions where more detailed datasets are available.

CRediT authorship contribution statement

Sebastiano Anselmo: Conceptualization, Data curation, Methodology, Software, Writing – original draft, Writing – review & editing. **Ana M. Martínez:** Conceptualization, Methodology, Supervision, Validation, Writing – review & editing. **Piero Boccardo:** Funding acquisition, Project administration, Supervision. **Maria Ferrara:** Supervision, Writing – review & editing.

Declaration of competing interest

The authors declare that they have no known competing financial interests or personal relationships that could have appeared to influence the work reported in this paper.

Acknowledgments

This paper reports part of the work developed within the project NODES, which has received funding from the MUR – M4C2 1.5 of PNRR with grant agreement no. ECS00000036. Further, this work was developed in accordance with the framework agreement between the City of Turin and the Polytechnic of Turin, signed on 9th February 2023 and renewed on 6th March 2025, for the realisation of pilot projects towards the implementation of a Digital Twin.

Data availability

Part of the raw data required to reproduce the above findings is available to download from dati.piemonte and Geoportale Piemonte. Additional data are property of the SDG11 Lab of the Politecnico di Torino. The Python code used for the research is available at https://github.com/anselmoseb/PV_AccuracyAssessment. The processed data required to reproduce the above findings will be made available upon request.

References

[1] G.H. Brundtland, Our Common Future—Call for Action, Environ. Conserv. 14 (4) (1987) 291–294, https://doi.org/10.1017/S0376892900016805.
[2] United Nations General Assembly, "Resolution adopted by the General Assembly on 25 September 2015," 2015.
[3] European Commission, "Communication from the Commission to the European Parliament, the Council, the European Economic and Social Committee and the Committee of the Regions. REPowerEU Plan," May 18, 2022, Brussels.
[4] European Commission, "Communication from the Commission to the European Parliament, the Council, the European Economic and Social Committee and the Committee of the Regions. EU Solar Energy Strategy," May 18, 2022, Brussels.
[5] European Parliament and Council, "Directive 2009/28/EC of the European and of the Council of 23 April 2009 on the promotion of the use of energy from renewable sources and amending and subsequently repealing Directives 2001/77/EC and 2003/30/EC," Apr. 23, 2009, Brussels.
[6] Council of the European Union, "Brussels European Council 8/9 March 2007 - Presidency conclusions (7224/1/07 Rev 1)," Mar. 2007, Brussels.
[7] Council of the European Union, "Fit for 55." Accessed: Feb. 02, 2024. [Online]. Available: https://www.consilium.europa.eu/en/policies/green-deal/fit-for-55-the-eu-plan-for-a-green-transition/.
[8] European Commission, "The European Green Deal." Accessed: Feb. 27, 2024. [Online]. Available: https://commission.europa.eu/strategy-and-policy/priorities-2019-2024/european-green-deal_en.
[9] European Parliament and Council, "Directive (EU) 2018/2001 of the European Parliament and of the Council of 11 December 2018 on the promotion of the use of energy from renewable sources (recast)," Dec. 11, 2018.
[10] European Parliament and Council, "Proposal for a Directive of the European Parliament and of the Council on the energy performance of buildings (recast)," Dec. 15, 2021.
[11] Y. Zhou, D. Wilmink, M. Zeman, O. Isabella, H. Ziar, A geographic information system-based large scale visibility assessment tool for multi-criteria photovoltaic planning on urban building roofs, Renew. Sustain. Energy Rev. 188 (Dec. 2023) 113885, https://doi.org/10.1016/j.rser.2023.113885.
[12] S. Anselmo, M. Ferrara, Trends and Evolution of the GIS-Based Photovoltaic potential Calculation, Energies (Basel) 16 (23) (2023) 7760, https://doi.org/10.3390/en16237760.
[13] M.S. Wong, et al., Estimation of Hong Kong's solar energy potential using GIS and remote sensing technologies, Renew. Energy 99 (2016) 325–335, https://doi.org/10.1016/j.renene.2016.07.003.
[14] F. Nex et al., "3D SolarWeb: A solar cadaster in the Italian alpine landscape," in International Archives of the Photogrammetry, Remote Sensing and Spatial Information Sciences - ISPRS Archives, 2013, pp. 173–178. doi: 10.5194/isprsarchives-XL-7-W2-173-2013.
[15] N. Sarmiento, S. Belmonte, P. Dellicompagni, J. Franco, K. Escalante, J. Sarmiento, A solar irradiation GIS as decision support tool for the Province of Salta, Argentina, Renew. Energy 132 (2019) 68–80, https://doi.org/10.1016/j.renene.2018.07.081.
[16] G. Desthieux, et al., Solar Energy potential Assessment on Rooftops and Facades in Large built Environments based on LiDAR Data, image Processing, and Cloud Computing. Methodological Background, Application, and Validation in Geneva (Solar Cadaster), Front. Built Environ. 4 (2018), https://doi.org/10.3389/fbuil.2018.00014.
[17] G. Agugiaro, F. Remondino, G. Stevanato, R. De Filippi, and C. Furlanello, "Estimation of solar radiation on building roofs in mountainous areas," The International Archives of the Photogrammetry, Remote Sensing and Spatial Information Sciences, vol. 38, no. 3W22, pp. 155–160, Apr. 2013, doi: 10.5194/isprsarchives-XXXVIII-3-W22-155-2011.
[18] S. Anselmo, A. Safaeianpour, S.T. Moghadam, M. Ferrara, GIS-based solar radiation modelling for photovoltaic potential in cities: a sensitivity analysis for the evaluation of output variability range, Energy Rep. 12 (2024) 4656–4669, https://doi.org/10.1016/j.egyr.2024.10.031.
[19] K. Bódis, I. Kougias, A. Jäger-Waldau, N. Taylor, S. Szabó, A high-resolution geospatial assessment of the rooftop solar photovoltaic potential in the European Union, Renew. Sustain. Energy Rev. 114 (2019) 109309, https://doi.org/10.1016/j.rser.2019.109309.
[20] M.-L. Tseng, N. Eshaghi, A. Gassoumi, M.M. Dehkalani, N.E. Gorji, Experimental measurements of soiling impact on current and power output of photovoltaic panels, Mod. Phys. Lett. B 37 (34) (2023) Dec, https://doi.org/10.1142/S0217984923501828.
[21] B. Kausika, W. van Sark, Calibration and Validation of ArcGIS Solar Radiation Tool for Photovoltaic potential Determination in the Netherlands, Energies (Basel) 14 (7) (2021) 1865, https://doi.org/10.3390/en14071865.
[22] K. Suomalainen, V. Wang, B. Sharp, Rooftop solar potential based on LiDAR data: Bottom-up assessment at neighbourhood level, Renew. Energy 111 (2017) 463–475, https://doi.org/10.1016/j.renene.2017.04.025.
[23] S. Özdemir, A. Yavuzdoğan, B.B. Bilgilioğlu, Z. Akbulut, SPAN: an open-source plugin for photovoltaic potential estimation of individual roof segments using point cloud data, Renew. Energy 216 (2023) 119022, https://doi.org/10.1016/j.renene.2023.119022.
[24] A.A. Bayod-Rújula, A. Ortego-Bielsa, A. Martínez-Gracia, Photovoltaics on flat roofs: Energy considerations, Energy 36 (4) (2011) 1996–2010, https://doi.org/10.1016/j.energy.2010.04.024.
[25] Y. Choi, J. Rayl, C. Tammineedi, J.R.S. Brownson, PV Analyst: Coupling ArcGIS with TRNSYS to assess distributed photovoltaic potential in urban areas, Sol. Energy 85 (11) (2011) 2924–2939, https://doi.org/10.1016/j.solener.2011.08.034.
[26] J.-Y. Han, Y.-C. Chen, S.-Y. Li, Utilising high-fidelity 3D building model for analysing the rooftop solar photovoltaic potential in urban areas, Sol. Energy 235 (2022) 187–199, https://doi.org/10.1016/j.solener.2022.02.041.
[27] J. Hofierka, J. Kaňuk, Assessment of photovoltaic potential in urban areas using open-source solar radiation tools, Renew. Energy 34 (10) (2009) 2206–2214, https://doi.org/10.1016/j.renene.2009.02.021.

[28] G. Mutani, M. Casalengo, and M. A. Ramassotto, "The effect of roof-integrated solar technologies on the energy performance of public buildings : the case study of the City of Turin (IT)," in INTELEC, International Telecommunications Energy Conference (Proceedings), 2019. doi: 10.1109/INTLEC.2018.8612398.
[29] M. Helbich, A. Jochem, W. Mücke, B. Höfle, Boosting the predictive accuracy of urban hedonic house price models through airborne laser scanning, Comput. Environ. Urban Syst. 39 (2013) 81–92, https://doi.org/10.1016/j.compenvurbsys.2013.01.001.
[30] J. Khan, M.H. Arsalan, Estimation of rooftop solar photovoltaic potential using geo-spatial techniques: a perspective from planned neighborhood of Karachi – Pakistan, Renew. Energy 90 (2016) 188–203, https://doi.org/10.1016/j.renene.2015.12.058.
[31] E. Achbab, R. Lambarki, H. Rhinane, and D. Saifaoui, "Estimation of photovoltaic potential at the urban level from 3d city model (solar cadaster): Case of casablanca city, morocco," in International Archives of the Photogrammetry, Remote Sensing and Spatial Information Sciences – ISPRS Archives, vol. 46, 2022, pp. 9–16. doi: 10.5194/isprs-archives-XLVI-4-W3-2021-9-2022.
[32] H. Saadaoui, A. Ghennioui, B. Ikken, H. Rhinane, and M. Maanan, "Using GIS and photogrammetry for assessing solar photovoltaic potential on Flat Roofs in urban area case of the city of Ben Guerir / Morocco," in International Archives of the Photogrammetry, Remote Sensing and Spatial Information Sciences - ISPRS Archives, vol 42, 2019, pp. 155–166. doi: 10.5194/isprs-archives-XLII-4-W12-155-2019.
[33] P. Soares, M. Bayrakci-Boz, and J. R. S. Brownson, "GIS Information for Solar PV Energy Siting: A Case Study in the Borough of State College, PA, USA," in Conference Record of the IEEE Photovoltaic Specialists Conference, 2020, pp. 1749–1753. doi: 10.1109/PVSC45281.2020.9300797.
[34] J. K. Kazak and M. Świąder, "SOLIS - A novel decision support tool for the assessment of solar radiation in ArcGIS," Energies (Basel)., vol. 11, no. 8, 2018, doi: 10.3390/en11082105.
[35] S. HosseiniHaghighi, P.M.Á. de Uribarri, R. Padsala, U. Eicker, Characterizing and structuring urban GIS data for housing stock energy modelling and retrofitting, Energ. Buildings 256 (2022), https://doi.org/10.1016/j.enbuild.2021.111706.
[36] R. Mahtta, P.K. Joshi, A.K. Jindal, Solar power potential mapping in India using remote sensing inputs and environmental parameters, Renew. Energy 71 (2014) 255–262, https://doi.org/10.1016/j.renene.2014.05.037.
[37] M.A. Green, et al., Solar Cell Efficiency Tables (Version 66), Prog. Photovolt. Res. Appl. 33 (7) (2025) 795–810, https://doi.org/10.1002/pip.3919.
[38] J. Liu, et al., A novel approach for assessing rooftop-and-facade solar photovoltaic potential in rural areas using three-dimensional (3D) building models constructed with GIS, Energy 282 (2023) 128920, https://doi.org/10.1016/J.ENERGY.2023.128920.
[39] D. Giannelli, C. León-Sánchez, and G. Agugiaro, "Comparison and Evaluation of Different GIS Software Tools to Estimate Solar Irradiation," ISPRS Annals of the Photogrammetry, Remote Sensing and Spatial Information Sciences, vol. V-4–2022, pp. 275–282, May 2022, doi: 10.5194/isprs-annals-V-4-2022-275-2022.
[40] Y.A. Eltbaakh, M.H. Ruslan, M.A. Alghoul, M.Y. Othman, K. Sopian, T.M. Razykov, Solar attenuation by aerosols: an overview, Renew. Sustain. Energy Rev. 16 (6) (2012) 4264–4276, https://doi.org/10.1016/j.rser.2012.03.053.
[41] H. D. Kambezidis, "The Solar Resource," in Comprehensive Renewable Energy, Elsevier, 2022, pp. 26–117. doi: 10.1016/B978-0-12-819727-1.00002-9.
[42] J. Remund, L. Wald, M. Levèvre, T. Ranchin, and J. H. Page, "Worldwide Linke turbidity information," in ISES Solar World Congress 2003, Goteborg, Sweden, Jun. 2003.
[43] J. K. Page, "Radiation Data," in Solar Energy Conversion II, Elsevier, 1981, pp. 23–35. doi: 10.1016/B978-0-08-025388-6.50013-1.
[44] C. Rigollier, O. Bauer, L. Wald, On the clear sky model of the ESRA — European Solar Radiation Atlas — with respect to the heliosat method, Sol. Energy 68 (1) (2000) 33–48, https://doi.org/10.1016/S0038-092X(99)00055-9.
[45] F. Kasten, The linke turbidity factor based on improved values of the integral Rayleigh optical thickness, Sol. Energy 56 (3) (1996) 239–244, https://doi.org/10.1016/0038-092X(95)00114-7.
[46] J. Hofierka, M. Suri, and T. Huld, "r.sun - GRASS GIS manual." Accessed: Nov. 01, 2023. [Online]. Available: https://grass.osgeo.org/grass83/manuals/r.sun.html.
[47] European Commission, "PVGIS 5.3." Accessed: Dec. 27, 2025. [Online]. Available: https://joint-research-centre.ec.europa.eu/photovoltaic-geographical-information-system-pvgis/pvgis-releases/pvgis-53_en.
[48] Solar Energy Services for Professionals, "SoDa." Accessed: Oct. 11, 2023. [Online]. Available: https://www.soda-pro.com/.
[49] S.A. Klein, Calculation of monthly average insolation on tilted surfaces, Sol. Energy 19 (4) (1977) 325–329, https://doi.org/10.1016/0038-092X(77)90001-9.
[50] G. Kakoulaki, et al., Mapping Europe's rooftop photovoltaic potential with a building-level database, Nat. Energy 11 (2026), https://doi.org/10.1038/s41560-025-01947-x.
[51] T. Muneer, Solar radiation model for Europe, Build. Serv. Eng. Res. Technol. 11 (4) (1990) 153–163, https://doi.org/10.1177/014362449001100405.
[52] R. Perez, P. Ineichen, E. L. Maxwell, R. D. Seals, and A. Zelenka, " Dynamic Models for hourly globalto-direct irradiance conversion," in Solar World Congress 1991, Denver, Colorado: International Solar Energy Society, 1991.
[53] B. Ridley, J. Boland, P. Lauret, Modelling of diffuse solar fraction with multiple predictors, Renew. Energy 35 (2) (2010) 478–483, https://doi.org/10.1016/j.renene.2009.07.018.
[54] Solar Energy Services for Professionals, "Linke turbidity factor - SoDa." Accessed: Feb. 15, 2024. [Online]. Available: https://www.soda-pro.com/help/general-knowledge/linke-turbidity-factor.
[55] J. Remund, S. Müller, M. Schmutz, D. Barsotti, P. Graf, and R. Cattin, "Handbook part I: Software," in Meteonorm 8. Irradiation data for every place on Earth, Bern: Meteotest AG, 2023, pp. 1–81.
[56] P. Fu and P. Rich, "Design and implementation of the Solar Analyst: an ArcView extension for modeling solar radiation at landscape scales," Proceedings of the 19th Annual ESRI User Conference, Feb. 1999.
[57] G. V. Fracastoro, Y. Yang, M. Simonetti, and G. Coppa, "Atmospheric Turbidity Measurements in Torino: A Comparison Between 1975 and 2010 Data," in Proceedings of the ISES Solar World Congress 2011, Freiburg, Germany: International Solar Energy Society, 2011, pp. 1–9. doi: 10.18086/swc.2011.24.11.